Small

NANO · MICRO small
www.small-journal.com

RESEARCH ARTICLE

Stabilizing Lattice Oxygen Redox Through Bicarbonate Pyrolysis-Driven Multifunctional Interface Engineering in Li-Rich Layered Oxides

Hongyu Zhu[1] | Shaoyun Yang[1] | Lu Lu[1] | Jiangnan Ke[1] | Yunsheng Zhang[1] | Wei Zeng[1] | Xiulin Yang[1] | Tayirjan Taylor Isimjan[2] | Bao Wang[3] | Xijie Lin[1]

[1]Guangxi Key Laboratory of Low Carbon Energy Materials, School of Chemistry and Pharmaceutical Sciences, Guangxi Normal University, Guilin, China | [2]Saudi Arabia Basic Industries Corporation (SABIC) At King Abdullah University of Science and Technology (KAUST), Thuwal, Saudi Arabia | [3]CAS Center for Excellence in Nanoscience, Institute of Process Engineering, Chinese Academy of Sciences, Beijing, China

Correspondence: Xiulin Yang (xlyang@gxnu.edu.cn) | Bao Wang (baowang@ipe.ac.cn) | Xijie Lin (linxijie@mailbox.gxnu.edu.cn)

Received: 4 February 2026 | **Revised:** 18 May 2026 | **Accepted:** 9 June 2026

Keywords: bicarbonate pyrolysis | cycling stability | high-energy density | interface engineering | Li-rich layered oxides | lithium-ion batteries

ABSTRACT

Li-rich layered oxides (LRs) are promising candidates for high-capacity cathodes in next-generation lithium-ion batteries (LIBs). However, their commercialization faces challenges such as rapid capacity fading, voltage decay, and irreversible oxygen release. In this study, we develop an innovative interface engineering driven by bicarbonate pyrolysis, which constructs a coherent spinel-phase surface layer, generates abundant oxygen vacancies, and facilitates near-surface metal ion doping (K^+, Na^+, or Mg^{2+}) on LRs. These enhancements work synergistically to significantly boost the electrochemical performance of the cathode. Notably, the optimized $KHCO_3$-treated sample (SK-LR) exhibits outstanding cycling stability, retaining 94.9% of its capacity after 500 cycles at 1C and 98.9% after 100 cycles at 0.1C, compared to only 67.8% and 85.5% retention for the pristine cathode. Furthermore, SK-LR achieves a high energy density of 1 110.5 Wh kg^{-1}, along with superior rate capability and thermal stability. Through ex/in situ characterizations and theoretical calculations, this interface engineering is evidenced to be effectively stabilize lattice oxygen by increasing oxygen vacancy formation energy from 3.87 to 5.34 eV, enhancing crystal structure via strengthened Mn—O bonds, and optimizing Li^+/e^- transport kinetics. This work presents effective interfacial engineering to develop ultra-stable Li-rich cathodes, offering a viable pathway for advancing high-energy density LIBs.

1 | Introduction

The rapid growth of electric vehicles, portable electronics, and grid-scale energy storage systems has sharply increased the demand for lithium-ion batteries (LIBs) with higher energy density and longer cycle life, thereby driving the development of advanced cathode materials [1, 2]. Conventional cathodes such as $LiCoO_2$, $LiNi_{0.5}Mn_{1.5}O_4$, and $LiFePO_4$, are increasingly constrained by their limited specific capacities, which fail to meet the performance requirements of next-generation LIBs. In this context, Li-rich layered oxides (LRs), typically described as $xLi_2MnO_3 \cdot (1\text{-}x)LiMO_2$ (M = Ni, Co, Mn, $0 < x < 1$), have emerged as promising cathode candidates due to their high specific capacity ($\geq$ 250 mAh g^{-1}), elevated operating voltage ($\geq$ 3.5 V vs. Li/Li^+), and cost advantage [3, 4]. Their ultrahigh specific capacity arises from the synergistic participation of both transition metal cations and oxygen anions in redox reactions, providing marked performance advantages over conventional cathodes [5, 6]. Despite these merits, the practical application of LRs is severely impeded by several challenges, including low

initial Coulombic efficiency (ICE), severe capacity degradation, poor rate capability, and continuous voltage fading and hysteresis during cycling [7, 8].

The oxygen anionic redox process, while contributes to the superior specific capacity, simultaneously initiates a cascade of detrimental effects that compromise battery performance [9, 10]. During the initial charging process, the irreversible release of oxygen from the crystal lattice drives the migration of transition metal (TM) ions into the adjacent Li^+ sites, which reduces active sites number available for Li^+ intercalation, thereby leading to a low ICE [11]. The TM ions migration also triggers a structural transformation from the original layered phase to spinel and/or rock-salt phases, which is directly responsible for the capacity degradation and voltage decay [12, 13]. In addition, the intrinsically sluggish kinetics of the anionic redox reaction, compared to cationic redox, adversely impact the rate capability of LRs [14]. Furthermore, side reactions between the highly oxidized cathode surface and the electrolyte not only deplete the accessible Li^+ ions but also lead to the formation of a passivation layer that hinders Li^+ diffusion, which further accelerates capacity loss [15]. Besides, repeated lithiation/delithiation cycles induce internal lattice strain and microcracks, facilitating electrolyte penetration and accelerating parasitic reactions, which result in structural degradation [16–18].

Extensive studies have established that the structural degradation of LRs typically initiates at the surface and subsequently propagates into the bulk phase [19]. Moreover, while the oxygen anionic redox in the bulk is largely reversible, these reactions at the surface often tend to cause irreversible oxygen release, further aggravating structural instability [20]. Accordingly, interface engineering has proven crucial for enhancing the performance of LRs. Surface coating is a widely adopted strategy due to its effectiveness in mitigating interfacial issues [21, 22]. However, conventional coatings often suffer from weak interaction with the host material, resulting in inadequate protection [23]. To address this limitation, Pan et al. demonstrated that pre-introduced oxygen vacancies could in situ induce a spinel phase layer, which achieved coherent lattice matching with the layered bulk structure of LRs [24]. This spinel layer not only stabilized the interface but also provided 3D pathways that promoted Li^+ transport [25]. Moreover, the introduced oxygen vacancies helped modulate the local electronic structure of the cathode, thereby enhancing both electronic conductivity and rate capability [26]. Given the multifaceted nature of LRs degradation, element doping is often integrated with surface engineering to synergistically improve cathode performance [27]. By strengthening the TM—O bonds, doping effectively suppresses lattice oxygen loss and improves structural stability [28]. Despite these insights, the rational design and practical fabrication of such a hierarchically modified structure continue to pose a significant challenge.

In this study, we develop an innovative interface engineering strategy driven by metal bicarbonate ($KHCO_3$, $NaHCO_3$, or $Mg(HCO_3)_2$) pyrolysis for $Li_{1.2}Mn_{0.54}Ni_{0.13}Co_{0.13}O_2$ cathode material. Specifically, the thermal decomposition of this metal bicarbonate triggers gas–solid interface reactions between the released CO_2 and the cathode surface. This process promotes the generation of oxygen and lithium vacancies, which subsequently facilitates the formation of a spinel phase layer and promotes the diffusion of metal ions (K^+, Na^+, or Mg^{2+}) into the near-surface region of the cathode material. Previous CO_2-driven surface modification strategies typically employed pure CO_2 gas or NH_4HCO_3 pyrolysis and mainly focus on generating vacancies and triggering surface phase transitions [29–31]. In contrast, the use of metal bicarbonate in our approach enables the simultaneous integration of oxygen vacancies, a spinel phase layer, and near-surface metal ions doping (K^+, Na^+, or Mg^{2+}) in a single and facile treatment process. Benefiting from these coupled effects, the modified cathode exhibits significantly enhanced cyclic stability and rate capability. Notably, the $KHCO_3$-treated sample delivers an ultrastable cycling performance, retaining 94.9% of its initial capacity after 500 cycles at 1C, far exceeding the 67.8% retention of the unmodified cathode. The mechanisms underlying this interface engineering are systematically elucidated through a combination of ex/in situ characterizations and theoretical calculations. The results highlight the effectiveness of this multifunctional interface engineering in improving interfacial stability, suppressing lattice oxygen release, enhancing Li^+ diffusion kinetics, and mitigating structural degradation. This work provides a promising interface engineering strategy for developing high-performance LRs, contributing to the advancement of high-energy density LIBs.

2 | Results and Discussion

2.1 | Bicarbonate Pyrolysis-Driven Strategy for Interface Engineering of LRs

To mitigate performance degradation in LRs, a bicarbonate pyrolysis-driven strategy is developed to construct a multifunctional interfacial structure on the $Li_{1.2}Mn_{0.54}Ni_{0.13}Co_{0.13}O_2$ cathode. As shown in Figure 1a, this structure incorporates a spinel phase layer, abundant oxygen vacancies, and near-surface metal ion doping. In a typical synthesis, the cathode powder and a selected bicarbonate ($KHCO_3$, $NaHCO_3$, or $Mg(HCO_3)_2$) are sealed in an argon-filled reaction vessel and heated at 200°C for 3 h. Upon heating, the bicarbonate decomposes, releasing CO_2 that initiates gas–solid interfacial reactions with the cathode surface. These reactions lead to the extraction of lattice oxygen from the subsurface region of the cathode, resulting in the generation of oxygen vacancies (OVs) [29]. Concurrently, lithium atoms on the cathode surface bond with the released CO_2, forming Li vacancies [30]. The coupled formation of Li/O vacancies induces a partial structural transformation from the layered to the spinel phase, while promoting the diffusion of metal ions (K^+, Na^+, or Mg^{2+}) from the decomposed bicarbonate into the near-surface region of the cathode. Collectively, these effects establish a multidimensional interface modification that significantly enhances the interfacial and structural stability of the cathode.

2.2 | Morphology and Structure Analysis

To illustrate the morphological and structural evolution of the cathode material after modification, the $KHCO_3$-treated $Li_{1.2}Mn_{0.54}Ni_{0.13}Co_{0.13}O_2$ (denoted as SK-LR) is selected as a representative example, with the pristine material (denoted as P-LR) serving as the comparison. As shown in Figure S1, scanning electron microscopy (SEM) images reveal that both samples consist

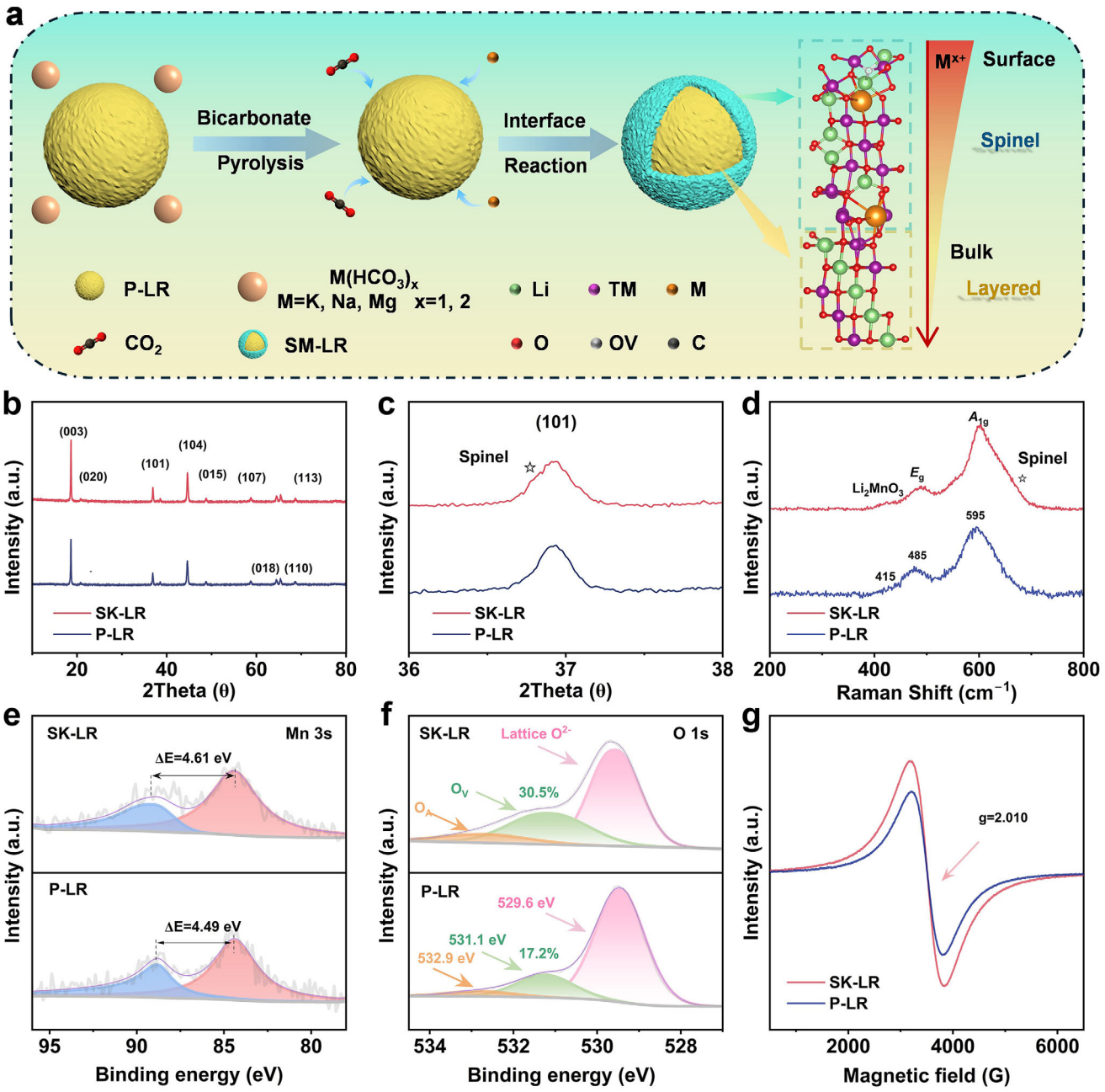

FIGURE 1 | (a) Schematic diagram of bicarbonate pyrolysis-driven interface engineering for $Li_{1.2}Mn_{0.54}Ni_{0.13}Co_{0.13}O_2$ cathode. (b) XRD patterns, (c) the magnified (101) diffraction peak of XRD patterns, (d) Raman spectra, (e) Mn 3s XPS spectra, (f) O 1s XPS spectra, and (g) EPR spectra of SK-LR and P-LR.

of microspherical particles, indicating that the treatment remains the overall morphology for the material. X-ray diffraction (XRD) is employed to analyze the phase composition of SK-LR and P-LR. Both their XRD patterns (Figure 1b) display characteristic diffraction peaks of the hexagonal $LiTMO_2$ phase (*R*-3*m* space group), along with weak peaks appearing around 20–25°, which are attributed to the monoclinic Li_2MnO_3 phase (*C*2/*m* space group). Notably, closer examination of the (101) diffraction peak (Figure 1c) reveals noticeable broadening in SK-LR compared to P-LR, suggesting the presence of a spinel phase (*Fd*-3*m* space group) in the modified sample. This broadening is due to the (311) diffraction peak of the spinel phase emerges around 36.8°, thereby contributing to the widening of the (101) reflection [32]. Rietveld refinements of the XRD patterns (Figure S2) further support these observations. Corresponding refinement results are provided in Table S1 and S2, which further demonstrate the formation of the spinel phase and oxygen vacancies after treatment. Furthermore, a *c*-axis expansion and an increase in unit cell volume are observed for SK-LR, primarily due to the incorporation of large-radius K^+ ions into the Li slabs [7, 24]. Additionally, the degree of Li/Ni cation mixing decreases from 2.23% in P-LR to 1.15% in SK-LR, indicating that the treatment effectively improves the structural ordering of the cathode. Lattice strain for P-LR and SK-LR samples is evaluated using the Williamson–Hall plot method, revealing a lattice strain value of 0.1619% for P-LR and 0.1889% for SK-LR (Figure S3). The increase in lattice strain in

SK-LR indicates that K^+ doping induces local lattice distortion, attributed to the ionic radius mismatch between K^+ and Li^+ [33]. The increased lattice strain, along with Li deficiency and oxygen vacancies that promote defect formation, also contributed to the lattice expansion observed in SK-LR.

Raman spectroscopy is employed to probe the surface fine structures of SK-LR and P-LR. As shown in Figure 1d, both samples display two characteristic peaks, with one at 485 cm^{-1} corresponding to the E_g mode (O—M—O bending) and the other at 595 cm^{-1} assigned to the A_{1g} mode (M—O stretching), both indicative of the layered $LiTMO_2$ phase with the *R*-3*m* space group [34]. A peak observed around 415 cm^{-1} is attributed to the A_g mode (phonon vibration) of the monoclinic Li_2MnO_3 phase with the *C*2/*m* space group [35]. Compared with P-LR, the A_{1g} vibration mode of SK-LR shows a redshift. Furthermore, a shoulder peak around 650 cm^{-1} is detected in SK-LR, which is ascribed to the Mn—O vibration of a cubic spinel phase with the *Fd*-3*m* space group, corroborating the formation of a spinel structure after treatment [36]. The surface chemical composition and valence states of SK-LR and P-LR are investigated using X-ray photoelectron spectroscopy (XPS). The comparison of the Ni 2p XPS spectra (Figure S4a) shows no significant change in binding energy after treatment, and a similar trend is observed in the Co 2p XPS spectra (Figure S4b), revealing that the valence states of Ni and Co in the cathode remain unchanged upon treatment. Moreover, the C 1s XPS spectra for both samples (Figure S4c) exhibit three peaks corresponding to C—C/C—H (284.8 eV), C—O (286.2 eV), and C═O (288.3 eV) [37]. The relative content of surface carbon species (C—O and C═O) is lower for SK-LR (24.81%) compared to P-LR (28.05%), indicating that the treatment effectively reduced carbon species residues on the surface of the treated sample. The Mn 3s XPS spectra are deconvoluted to determine the average oxidation state (AOS) of Mn. As shown in Figure 1e, the splitting energy (ΔE) is 4.61 eV for SK-LR and 4.49 eV for P-LR, respectively. Using the formula AOS = 8.956-1.126ΔE, the AOS of Mn decreases from +3.90 in P-LR to +3.77 in SK-LR, which is attributed to the formation of a spinel phase on the surface [38]. Although the valence of Mn decreases in SK-LR, the Jahn–Teller effect is not expected to occur since the AOS remains above +3.5 [39].

Figure 1f presents the O 1s XPS spectra for these two samples. Peaks located at 529.6, 531.1, and 532.7 eV are assigned to TM—O bonds, oxygen vacancies, and adsorbed oxygen species, respectively [30]. Compared to P-LR, the peak intensity at 531.1 eV increases from 17.2% to 30.5% in SK-LR, confirming that the formation of oxygen vacancies. This result is further supported by electron paramagnetic resonance (EPR) analysis. As shown in Figure 1g, both samples exhibit EPR signals at a g-factor of approximately 2.010, characteristic of oxygen vacancy [40]. The stronger EPR signal observed in SK-LR indicates a higher concentration of oxygen vacancies compared to P-LR. Furthermore, to clearly confirm the formation of oxygen vacancies, soft X-ray absorption spectroscopy (sXAS) measurement is conducted. As shown in Figure S5, the pre-edge peak splits into two signals due to crystal field splitting, labeled as t_{2g} and e_g [41, 42]. Typically, a weaker pre-edge peak intensity in the O K-edge spectrum indicates a higher oxygen vacancy concentration [43, 44]. Consistent with this, the reduced pre-edge peak intensity observed in SK-LR compared to P-LR suggests a higher oxygen vacancy concentration in the treated sample.

The detailed phase composition in the near-surface region of the material is investigated using high-resolution transmission electron microscopy (HRTEM) and fast Fourier transform (FFT). As shown in Figures 2a, P-LR exhibits a typical layered structure both on the surface and in the bulk phase, corresponding to the (003) plane of the *R*-3*m* phase or the (001) plane of the *C*/2*m* phase. In contrast, while SK-LR retains the layered phase in the bulk, a surface spinel layer approximately 4 nm thick (white region) is observed, characterized by a lattice spacing of 0.210 nm matching the (400) plane of the spinel structure (Figure 2b). Furthermore, TEM analysis is conducted on multiple randomly selected regions of the SK-LR sample to confirm the presence of the spinel phase. As shown in Figure S6, distinct lattice fringes corresponding to the spinel phase are consistently observed in the near-surface region across all analyzed areas. The FFT patterns obtained from these regions all display characteristic diffraction spots that match the spinel structure. Elemental mapping based on an energy-dispersive X-ray spectrometer (EDS) reveals a homogeneous distribution of all elements in SK-LR (Figure 2c). The exact concentration of K in SK-LR was measured using inductively coupled plasma-optical emission spectrometry (ICP-OES) and determined to be 0.86 wt.%, corresponding to a K/TM atomic ratio of 0.0243. Furthermore, according to the ICP-OES results, the Li content decreases from 10.67 wt.% in P-LR to 10.34 wt.% in SK-LR, indicating slight Li loss during the treatment process. This moderate Li extraction further induces surface structural transformation and K^+ doping. To further probe the distribution of K^+ ions, XPS depth profiling with Ar^+ etching is performed. As shown in Figure 2d, the gradient distribution of K^+ ions in SK-LR is evidenced by the K 2p signal, which decays progressively with increasing etching depth, demonstrating near-surface K^+ ions doping. Collectively, these analyses demonstrate that the bicarbonate pyrolysis process effectively integrates a spinel phase layer, abundant oxygen vacancies, and near-surface metal ion doping, thereby achieving multifunctional interface engineering in Li-rich cathodes.

Encouragingly, this bicarbonate pyrolysis-driven interface engineering strategy demonstrates excellent versatility. In addition to $KHCO_3$, other bicarbonates, such as $NaHCO_3$ and $Mg(HCO_3)_2$, can also be effectively employed in this method, as they similarly decompose to release CO_2 upon heating. However, due to differences in metal species, the use of $NaHCO_3$ and $Mg(HCO_3)_2$ results in different doping effects. The resulting cathodes prepared with these bicarbonates are labeled as SNa-LR and SMg-LR, respectively. SEM images (Figure S7) and XRD patterns (Figure S8) indicate that both modified materials retain the original morphological and structural characteristics. Similar to SK-LR, the (101) diffraction peak of SNa-LR and SMg-LR shows slight broadening, suggesting successful formation of a spinel phase. Furthermore, Raman spectra of the treated samples exhibit characteristic vibrations associated with $LiTMO_2$ and Li_2MnO_3, along with an additional Mn—O vibration signal attributable to the spinel phase (Figure S9). XPS analysis confirms the incorporation of Na^+ and Mg^{2+} ions into SNa-LR and SMg-LR, respectively, based on the detected Na 1s and Mg 1s signals. A gradient distribution of Na and Mg is also observed in SNa-LR and SMg-LR, supporting the near-surface metal ion doping

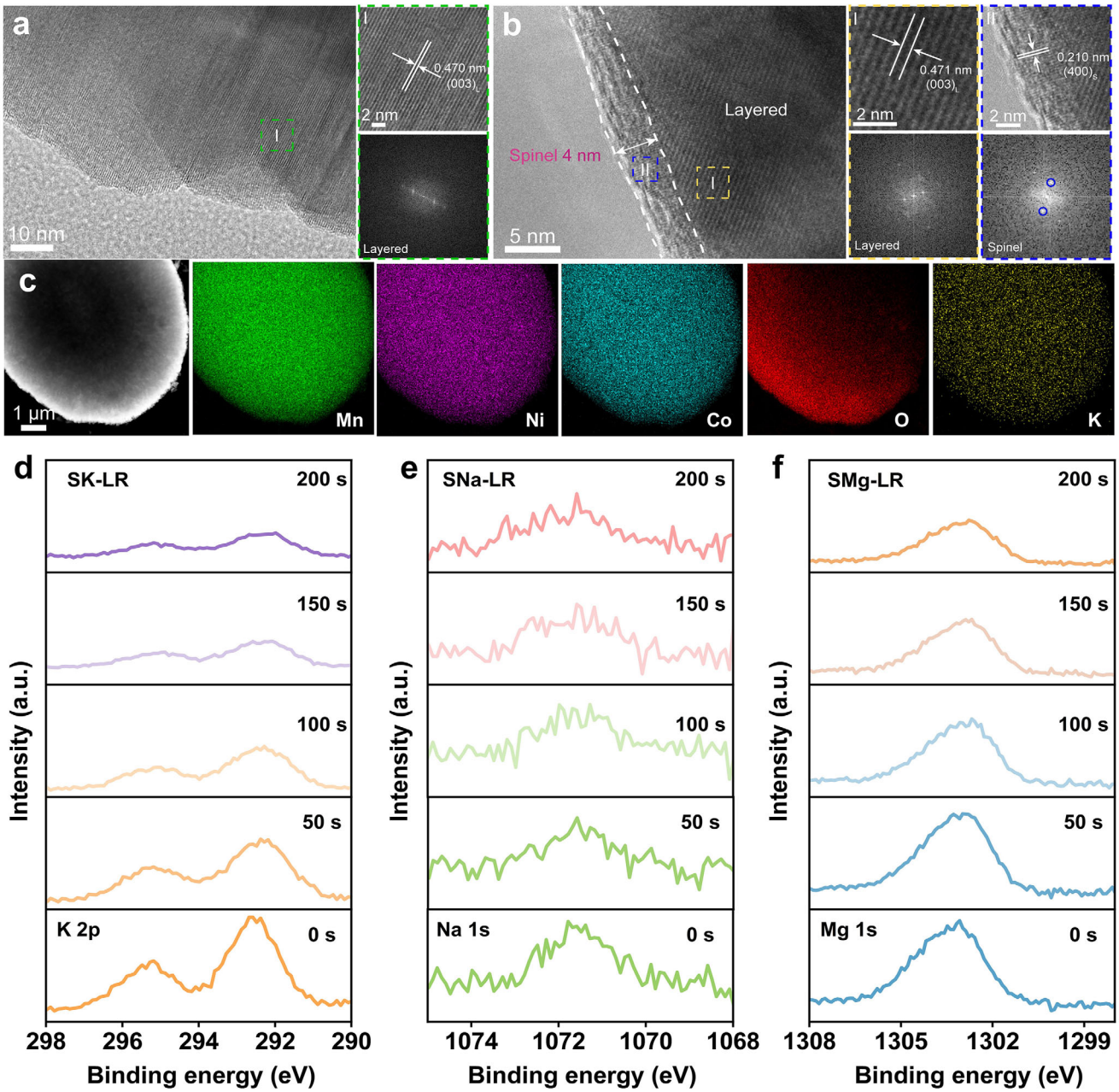

FIGURE 2 | HRTEM images and FFT patterns of (a) P-LR and (b) SK-LR. (c) Elemental mapping of SK-LR. (d) XPS etching profile of K 2p for SK-LR. XPS etching profile of (e) Na 1s for SNa-LR and (f) Mg 1s for SMg-LR.

(Figure 2e,f). However, the XPS etching profiles reveal distinct distribution behavior of K, Na, and Mg. While all three dopants exhibit near-surface doping characteristics, K demonstrates a steep decline in concentration at the surface, becoming very weak in the subsurface region. In contrast, Na and Mg exhibit a more gradual decrease, retaining relatively stronger signal intensities in the subsurface region. This discrepancy can be attributed to the difference in ionic radii. K^+ has the largest ionic radius (1.38 Å), which significantly hinders its inward diffusion, leading to strong surface localization. In comparison, Na^+ (1.02 Å) and Mg^{2+} (0.72 Å) possess smaller ionic radii, allowing for deeper incorporation into the subsurface. Analysis of the O 1s XPS spectra reveals an increased oxygen vacancy concentration in both modified samples compared to P-LR (17.2%), with calculated values reaching 23.3% for SNa-LR and 37.2% for SMg-LR (Figure S10a,b). These results are further corroborated by the enhanced EPR signals observed in both modified samples (Figure S10c).

2.3 | Electrochemical Performance Evaluation

To evaluate the impact of the bicarbonate pyrolysis-driven interface engineering on the lithium storage performance of LR, systematic electrochemical tests are conducted on both SK-LR and P-LR over a voltage range of 2.0-4.8 V (vs. Li/Li^+). Figure 3a,b present the initial charge–discharge profiles measured at 0.1C (1C = 250 mAh g^{-1}) and the corresponding dQ/dV curves. Both samples exhibit similar electrochemical behavior, with typical

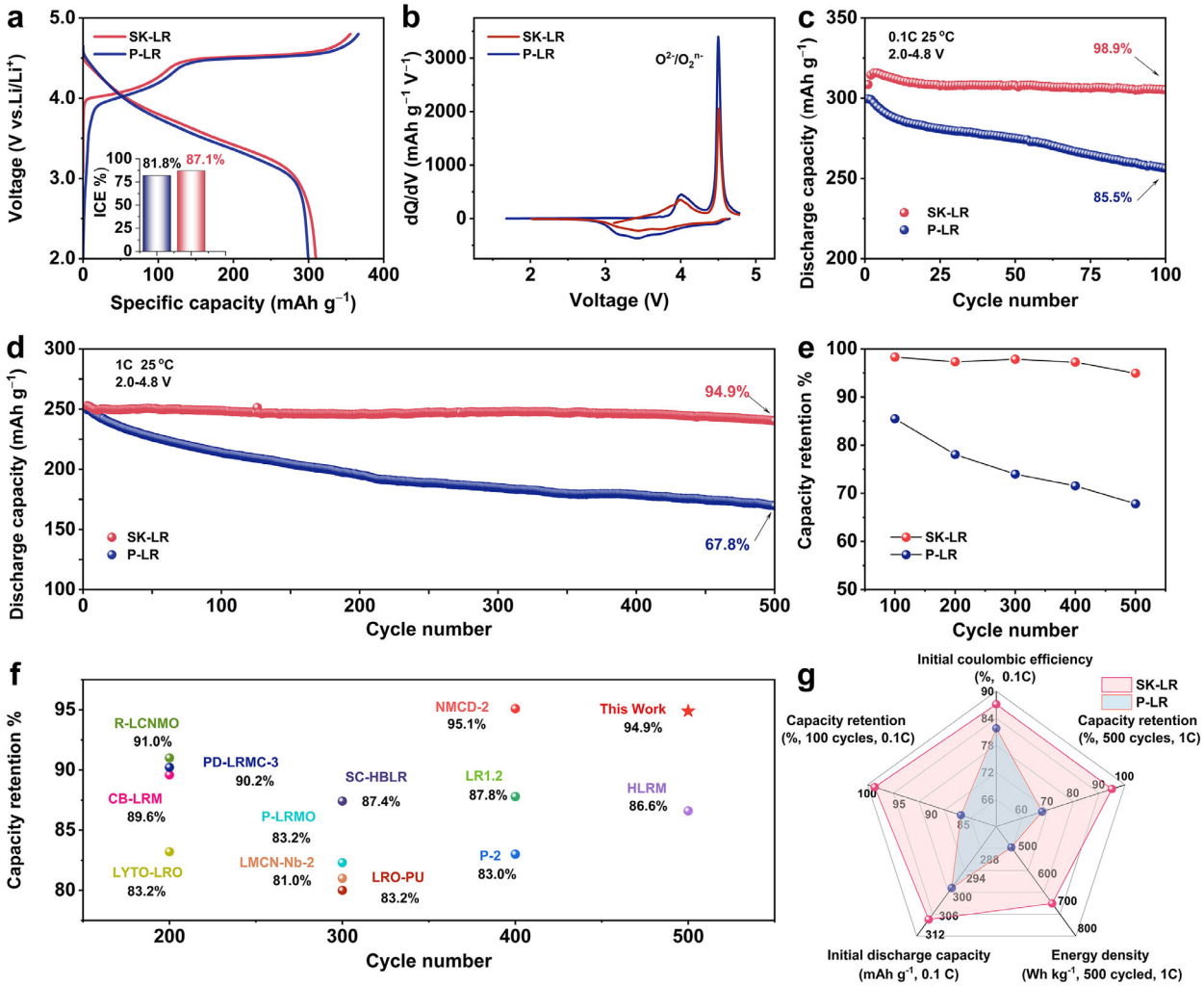

FIGURE 3 | (a) Initial charge–discharge profile at 0.1C and (b) the corresponding dQ/dV curves. Cycling performance at (c) 0.1C and (d) 1C. (e) Capacity retention evolution at 1C. (f) Comparison the cycling performance of SK-LR with other reported Li-rich cathodes. (g) Radar diagram for electrochemical performance comparison.

redox reactions of transition metal cations ($Ni^{2+}/Ni^{3+}/Ni^{4+}$, Co^{3+}/Co^{4+}, and Mn^{3+}/Mn^{4+}) and oxygen anions, consistent with the characteristic redox activities of Li-rich cathode materials [29, 36]. Notably, during the initial charging process, SK-LR shows a shortened plateau above 4.4 V, which is associated with the oxygen anionic oxidation, implying effective suppression of irreversible oxygen release [42]. Moreover, SK-LR delivers a higher discharge capacity of 309.72 mAh g^{-1} than that of P-LR (299.62 mAh g^{-1}), reflecting improved structural stability that facilitates more efficient Li^+ (de)intercalation. As a result, the initial Coulombic efficiency (ICE) of SK-LR increases significantly to 87.1%, compared to 81.8% for P-LR. Further evidence comes from the dQ/dV curves, in which the reduced peak intensity around 4.5 V for SK-LR indicates mitigated lattice oxygen loss. The enhanced discharge capacity and suppressed oxygen release in SK-LR are attributed to the multifunctional interface engineering, which effectively reduces the surface lattice oxygen reactivity, inhibits side reactions, and strengthens the metal-oxygen bonds.

Figure 3c compares the cycling performance of the SK-LR and P-LR cathodes at 0.1C for 100 cycles. The P-LR cathode delivers a discharge capacity of 256.32 mAh g^{-1} after cycling, corresponding to 85.5% retention of its initial capacity. In contrast, the SK-LR cathode demonstrates significantly improved cycling stability, maintaining a discharge capacity of 305.26 mAh g^{-1} after 100 cycles, with a capacity retention as high as 98.9%. The long-term cycling performance is further evaluated at 1C over 500 cycles. As shown in Figure 3d,e, SK-LR exhibits exceptional cyclic stability with an ultrahigh capacity retention of 94.9%, experiencing only a minimal capacity loss of 12.79 mAh g^{-1}. By comparison, P-LR suffers from severe capacity fading, with a capacity reduction of 80.26 mAh g^{-1} and a final retention of only 67.8% after 500 cycles. The charge-discharge profiles at selected cycles further confirm the effective suppression of capacity fading in the modified sample (Figure S11a,b). The discharge-voltage retention curves for both samples are presented in Figure S11c, illustrating that SK-LR exhibits a slight reduction in voltage decay (2.36 mV/cycle) compared to P-LR (2.63 mV/cycle) over 200 cycles. However, SK-LR does not demonstrate a significant reduction in voltage decay compared to P-LR. This can be attributed to the focus of the modification strategy on cathode interfacial engineering, which, although effective in enhancing interface stability, has limited capacity to regulate the bulk oxygen-redox processes closely associated with voltage decay [45].

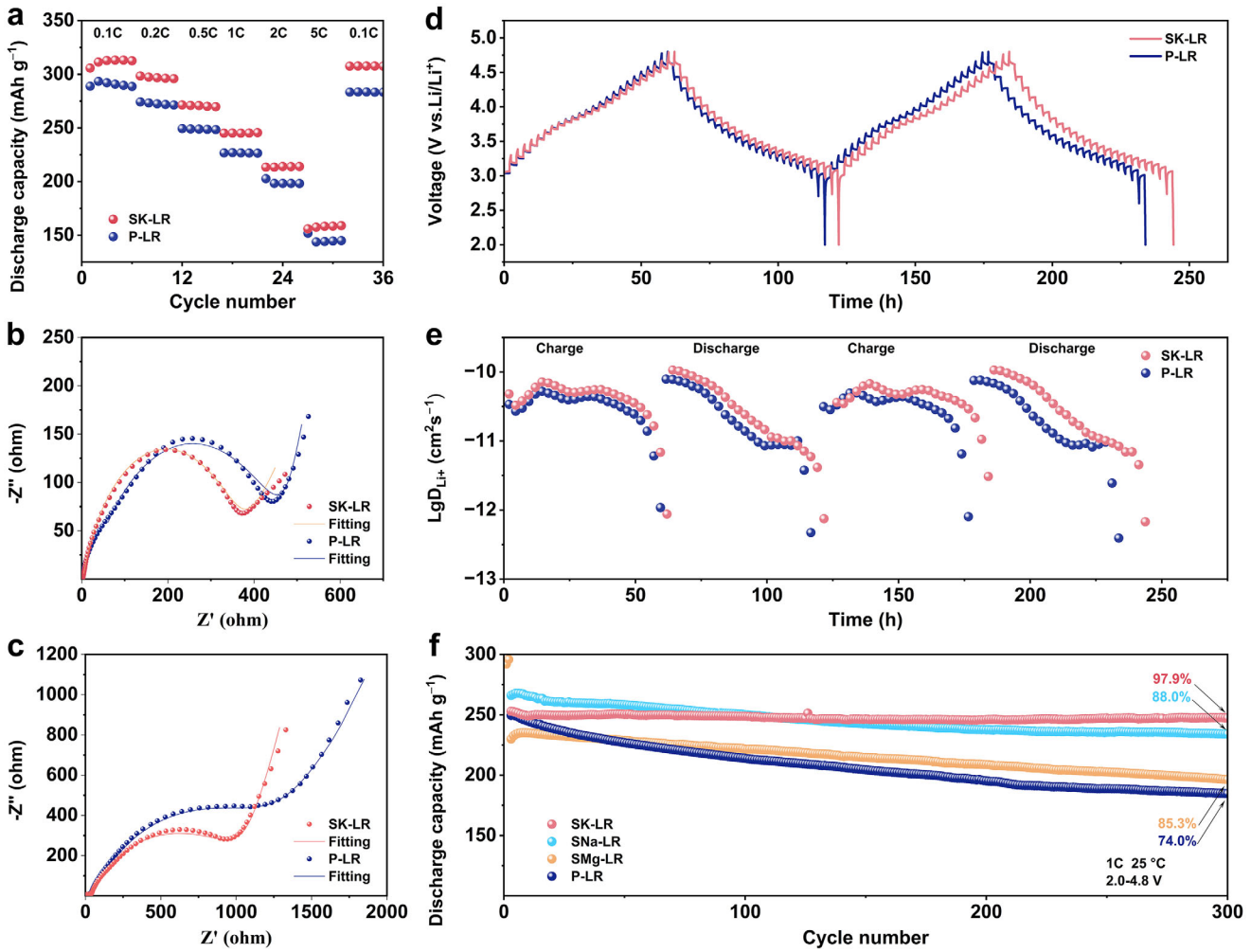

FIGURE 4 | (a) Rate performance, Nyquist plots recorded (b) before and (c) after cycling, (d) GITT curve, and (e) corresponding calculated Li^+ diffusion coefficients of SK-LR and P-LR. (f) Cycling performance of SK-LR, SNa-LR, SMg-LR, and P-LR.

The cycling performance of SK-LR is also benchmarked against other reported Li-rich cathodes. As summarized in Figure 3f and Table S3, the comparison clearly demonstrates the superior cycling stability of our modified material. In addition, SK-LR achieves a high energy density of 1 110.50 Wh kg^{-1}, which remains at 680.79 Wh kg^{-1} after 500 cycles, significantly higher than the 475.78 Wh kg^{-1} of cycled P-LR (Figure S12). A comprehensive performance comparison between SK-LR and P-LR is presented in the radar chart in Figure 3g, which incorporates key metrics such as ICE, initial discharge capacity at 0.1C, capacity retention at various current densities, and energy density. This visualization underscores the overall superiority of SK-LR and highlights its strong potential for advancing high-energy density LIBs.

The rate capabilities of the SK-LR and P-LR cathodes are compared in Figure 4a. SK-LR exhibits higher discharge capacities than P-LR across all current densities. Notably, at high rates of 2C and 5C, SK-LR delivers discharge capacities of 214.00 and 158.90 mAh g^{-1}, respectively, significantly surpassing those of P-LR (198.26 and 145.01 mAh g^{-1}). This enhanced rate performance originates from the synergistic effects of the spinel phase with 3D Li^+ diffusion channels, abundant oxygen vacancies, and strengthened K—O bonds in the modified cathode, which collectively facilitate rapid Li^+ transport. The charge transfer kinetics are further investigated using electrochemical impedance spectroscopy (EIS). Nyquist plots of both cathodes before and after 500 cycles at 1C are presented in Figure 4b,c, with the corresponding equivalent circuit and fitting parameters provided in Figure S13 and Table S4, respectively. The charge transfer resistance (R_{ct}) of P-LR increases markedly from 443.6 to 1 188.0 Ω after cycling. In contrast, SK-LR exhibits consistently lower R_{ct} values, rising only from 354.2 to 820.1 Ω after the same cycling period. An additional semicircle emerges in the high-frequency region after cycling for both samples, which is ascribed to the cathode/electrolyte interface impedance (R_{CEI}). The R_{CEI} value of SK-LR (26.14 Ω) is lower than that of P-LR (31.29 Ω), suggesting enhanced interfacial stability, likely resulting from the protective function of the spinel phase layer. The Li^+ diffusion coefficients ($D_{Li}{}^+$) are qualitatively assessed using the galvanostatic intermittent titration technique (GITT). As illustrated in Figure 4d,e and Table S5, SK-LR and P-LR exhibit similar $D_{Li}{}^+$ values during the first charge–discharge cycle, with SK-LR showing a slightly higher average $D_{Li}{}^+$. By the second cycle, the average $D_{Li}{}^+$ of P-LR decreases, whereas SK-LR maintains a higher average value, indicating more favorable and stable Li^+ diffusion kinetics.

The optimal dosage of $KHCO_3$ for modifying the LR cathode is investigated. LR treated with varying amounts of $KHCO_3$ are labeled as SK-LR-1 (3 wt.%), SK-LR (5 wt.%), and SK-LR-2 (7 wt.%), where the mass ratio is relative to the mass of the LR material. The exact amount of K in the cathode was measured using ICP-OES. The results indicated that the K concentration was 0.56wt.%, 0.86wt.%, and 0.97 wt.% for the SK-LR-1, SK-LR, and SK-LR-2 samples, respectively. As shown in Figure S14, the cycling performance of these $KHCO_3$-treated samples along with the P-LR is evaluated at 1C. All samples exhibit comparable initial discharge capacity, approximately 252.92 mAh g^{-1} for SK-LR, 249.85 mAh g^{-1} for SK-LR-1, 246.53 mAh g^{-1} for SK-LR-2, and 249.55 mAh g^{-1} for P-LR. After 500 cycles, SK-LR demonstrates the best cyclic stability with a capacity retention of 94.9%. SK-LR-2 also displays significantly improved performance compared to P-LR, retaining 85.5% of its initial capacity. In contrast, SK-LR-1 shows a capacity fading trend similar to that of P-LR, with retention of 70.3% and 67.8%, respectively. Based on these results, the optimal $KHCO_3$ dosage is determined to be 5 wt.% relative to the LR mass. To further assess the universality and feasibility of the bicarbonate pyrolysis-driven interface engineering strategy, the long-term cycling performance of LR cathodes treated with different bicarbonates is tested over 300 cycles at 1C. In line with the optimized $KHCO_3$ dosage, equivalent mass ratios relative to LR are also applied for $NaHCO_3$ and $Mg(HCO_3)_2$. The Na concentration in SNa-LR was measured to be 0.53 wt.% through ICP-OES, while the Mg concentration in SMg-LR was 0.79 wt.%. As illustrated in Figure 4f, all modified cathodes demonstrate significantly enhanced cycling stability compared to the untreated P-LR. Among them, SK-LR delivers the highest capacity retention of 97.9%, follows by 88.0% for SNa-LR and 85.3% for SMg-LR, all of which considerably exceed the 74.0% retention observed in P-LR. These results clearly confirm the effectiveness of the bicarbonate pyrolysis treatment in improving the electrochemical performance of Li-rich cathodes, underscoring the broad applicability and promising potential of this strategy for the optimization of next-generation high-capacity cathode materials.

2.4 | Structure and Morphology Evolution

The structural stability of the samples during charge-discharge cycling is evaluated using dQ/dV analysis and in situ XRD. Figure 5a,b displays selected dQ/dV curves measured at 1C. For SK-LR, the reduction peak corresponding to Mn^{4+}/Mn^{3+} and O_2^{n-}/O_2^{2-} shifts from 2.953 to 2.802 V, a displacement of 151 mV. In contrast, P-LR exhibits a more pronounced peak shift, from 2.976 to 2.719 V, corresponding to 257 mV. The smaller peak shift in SK-LR indicates improved crystal structure stability and suppressed oxygen loss after modification [32]. More detailed structural evolution is probed by in situ XRD during the first cycle at 0.15C. The charge–discharge profiles and corresponding contour plots for SK-LR and P-LR are presented in Figure 5c,d. Diffraction peak shifts are commonly used to assess structural stability and reversibility during cycling [46, 47]. Notably, the characteristic peaks of P-LR, including (003), (101), and (104), undergo larger shifts compared to SK-LR. For instance, the (003) peak shift is reduced to 0.168°, down from 0.262° observed in P-LR. Similar reductions are found for the (101) peak (from 0.245° to 0.171°) and the (104) peak (from 0.152° to 0.141°). These reduced shifts in SK-LR confirm significantly enhanced structural stability, which can be attributed to the reduced irreversible oxygen release by this multifunctional interfacial engineering. Lattice parameters, including *a*-axis, *c*-axis, and unit cell volume, are derived from Rietveld refinement of the XRD data. Both samples show similar patterns of expansion and shrinkage along the *c*-axis and *a*-axis during cycling. However, SK-LR exhibits smaller variations than P-LR. During charging, the Δc value for SK-LR is 1.02%, compared to a larger variation of 1.15% for P-LR. Moreover, the unit cell volume change in SK-LR is less pronounced throughout the entire process. The restrained variation in lattice parameters further demonstrates the efficacy of the interfacial engineering strategy in suppressing irreversible oxygen loss and phase transformation.

To further validate the reduction in gas emissions after modification, in situ differential electrochemical mass spectrometry (DEMS) is performed to monitor the gas evolution behavior of both SK-LR and P-LR during the first charge at 0.5C. As shown in Figure 5e, P-LR exhibits significant O_2 release, reaching a substantial amount of 0.35 nmol h^{-1}, indicating severe lattice oxygen loss. In contrast, almost no O_2 release is detected during the charging process of SK-LR (Figure 5f), confirming that irreversible lattice oxygen redox reactions are effectively suppressed through interface engineering. The excellent suppression of O_2 evolution observed in SK-LR can be attributed to both the physical barrier effect of the spinel layer and the thermodynamic stabilization of lattice oxygen, which arises from the synergistic effects of near-surface K^+ doping and the increased oxygen vacancy concentration. Similarly, SK-LR shows a marked reduction in CO_2 emissions compared to P-LR. Since CO_2 generation is generally attributed to the decomposition of surface residual lithium compounds and side reactions between the cathode and electrolyte, the lower CO_2 level observed for SK-LR suggests a decrease in residual lithium compounds and suppressed undesirable reactions at the cathode/electrolyte interface. These results further demonstrate the effectiveness of the multifunctional interfacial engineering in addressing crucial issues related to oxygen loss and structural instability in Li-rich cathodes. Consequently, the modified cathode exhibits significantly improved cycling performance and rate capability, along with enhanced safety due to reduced emission of flammable O_2. Furthermore, the thermal stability of both samples is evaluated using differential scanning calorimetry (DSC). The corresponding DSC curves are displayed in Figure 5g. As expected, SK-LR exhibits superior thermal stability compared to P-LR. An increase in the temperature of exothermic reactions from 397.26°C (P-LR) to 432.42°C (SK-LR) is observed, accompanied by a decrease in the total heat release from 731.31 to 628.98 J g^{-1}, further underscoring the efficacy of the modification in suppressing lattice oxygen release. Additionally, cycling performance is tested at an elevated temperature of 45°C (Figure 5h). At the higher operating temperature, both samples show improved discharge capacity. After 200 cycles, P-LR retained a capacity of 247.87 mAh g^{-1}, corresponding to a retention of 85.8%. Notably, SK-LR exhibits better stability under high-temperature cycling, achieving a higher capacity retention of 91.4%.

SEM and TEM analyses were performed to examine the morphological and surface structural changes of the cathodes after cycling. As shown in Figure S15a,b, the cycled P-LR displays extensive cracks and particle fragmentation. In contrast, SK-LR maintains their spherical morphology without visible cracks,

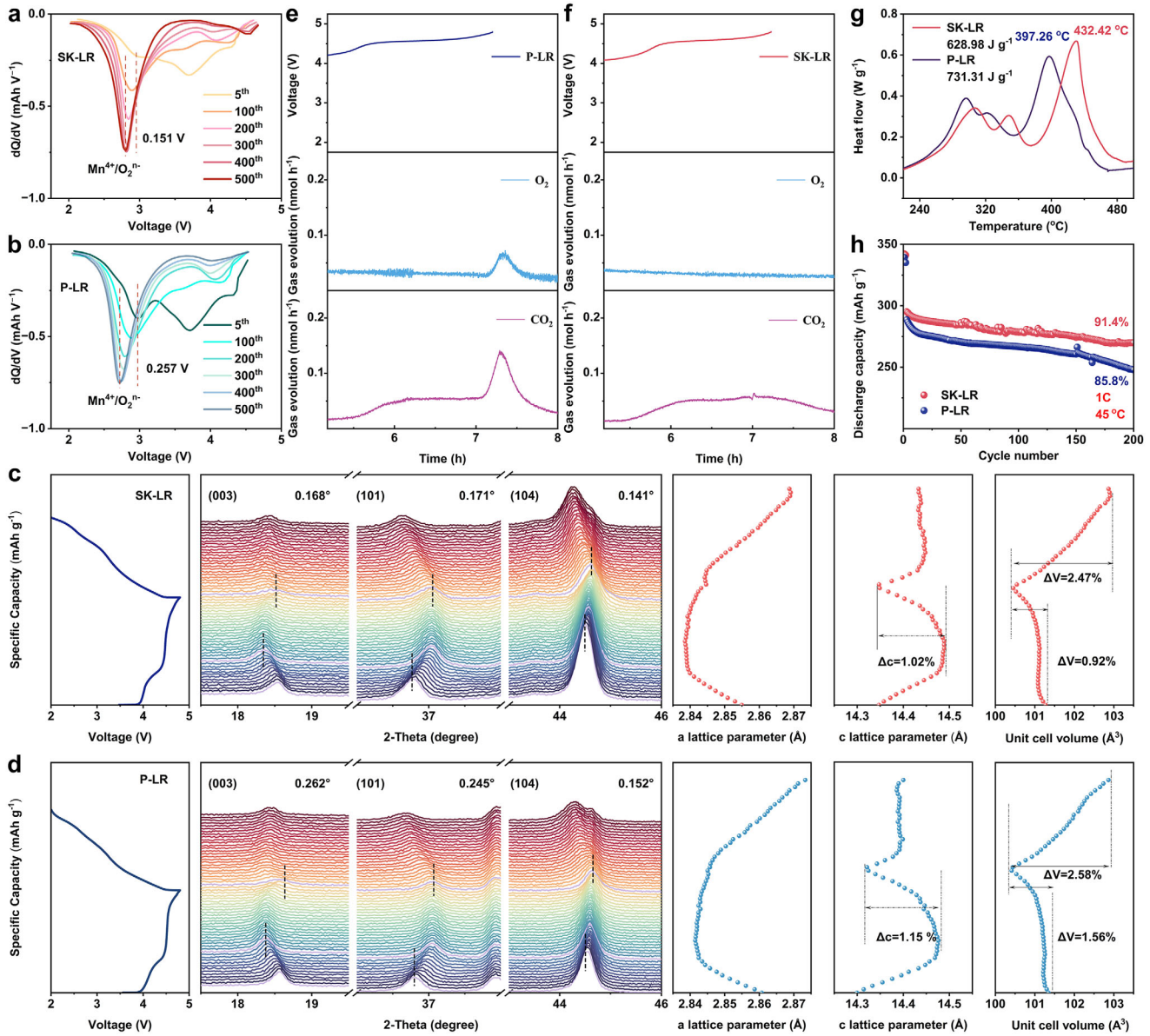

FIGURE 5 | dQ/dV profiles of (a) SK-LR and (b) P-LR. Charge-discharge profiles, contour plots of in situ XRD, and lattice parameter changes of (c) SK-LR and (d) P-LR. in situ DEMS tests during the first charging of (e) P-LR and (f) SK-LR. (g) DSC curves and (h) Cycling performance at 1C, 45°C within a 2.0–4.8 V voltage range of P-LR and SK-LR.

suggesting mitigated stress accumulation and improved structural integrity. XRD analysis is performed for both P-LR and SK-LR electrodes after 500 cycles at 1C, with results shown in Figure S16. After long-term cycling, the (003) diffraction peak of both samples has a shift. Specifically, P-LR exhibits a peak shift of 0.449°, which is significantly larger than the 0.113° for SK-LR, demonstrating that SK-LR undergoes much weaker lattice distortion and milder structural degradation during repeated cycling, in sharp contrast to the severe structural degradation of P-LR. HRTEM and FFT results further reveal severe surface degradation in P-LR, where a large region has transformed from the layered structure to the spinel-like phase (Figure S15c). In comparison, the cycled SK-LR largely retains the layered structure, with only a thin spinel layer detected at the surface (Figure S15d). The interface chemistry of the cycled cathodes is further probed by XPS analysis. Figure S17a,b present the high-resolution C 1s and F 1s XPS spectra of P-LR and SK-LR after 500 cycles at 1C. In the C 1s XPS spectra, both samples show four peaks corresponding to C—C/C—H, C—O, O—C═O, and C═O bonds. The C—C/C—H signal mainly comes from the binder and conductive additive, while the other three peaks indicate species formed by electrolyte decomposition at the cathode surface [48]. In the F 1s XPS spectra, the peak at 687.3 eV is attributed to polyvinylidene fluoride (PVDF). The peaks at 684.9 and 686.1 eV correspond to LiF and $Li_xPO_yF_z$/Li_xPO_y species, respectively, which are associated with electrolyte decomposition [49]. The lower intensity of these side-product-related peaks in SK-LR compared to P-LR confirms that the interfacial engineering effectively suppresses parasitic reactions between cathode and electrolyte.

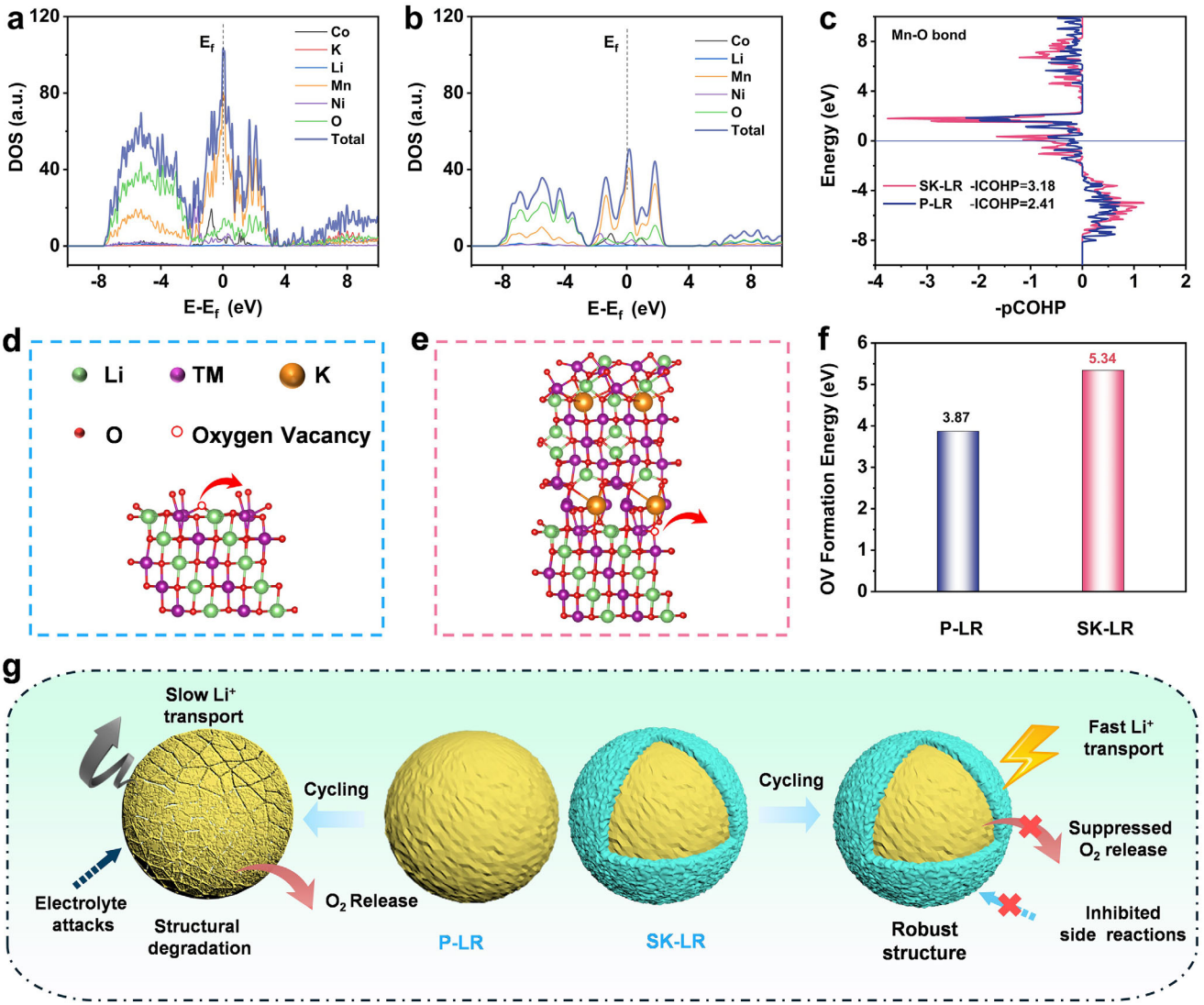

FIGURE 6 | Density of states profiles for (a) SK-LR and (b) P-LR. (c) COHP calculation of the Mn- O bond for SK-LR and P-LR. (d–f) Oxygen vacancy formation energy of P-LR and SK-LR. (g) Schematic diagram illustrating the mechanism of the multifunctional interfacial engineering strategy.

2.5 | Theoretical Calculation and Mechanism Investigation

To elucidate the mechanism underlying the performance improvements, density functional theory (DFT) calculations are carried out to investigate how the modification strategy influences the electronic structure, chemical bonding, and lattice oxygen stability. As depicted in Figure 6a,b, the density of states (DOS) of P-LR and SK-LR are compared. The enhanced peak intensity near the Fermi level in SK-LR relative to P-LR indicates improved electronic conductivity upon modification, which contributes to its superior rate performance [50]. Furthermore, Crystal Orbital Hamilton Population (COHP) calculations are performed on the Mn-O bond in both materials. As illustrated in Figure 6c, the higher integrated COHP (-ICOHP) value for SK-LR (3.18 eV) compared to P-LR (2.41 eV) reveals a strengthened Mn—O bond due to the multifunctional interfacial engineering. This reinforcement promotes enhanced reversibility of oxygen redox reactions and improves the structural flexibility of the crystal. The oxygen vacancy (OV) formation energy for both samples is compared in Figure 6d–f. Notably, SK-LR exhibits a higher formation energy of 5.34 eV versus 3.87 eV for P-LR, implying a greater energy barrier for oxygen release, which effectively suppresses lattice oxygen loss during cycling, thereby contributing to higher ICE and improved cycling stability. These computational results confirm that the presented interface engineering strategy effectively modulates the electronic structure and chemical bonding characteristics, leading to enhanced electronic conductivity, improved anionic redox reversibility, and a more stable crystal structure. A schematic illustration summarizing the mechanism of this multifunctional interface engineering is presented in Figure 6g. Benefitting from the incorporation of a spinel phase layer, abundant oxygen vacancies, and near-surface metal ion doping, the release of lattice oxygen is effectively inhibited, while the transport of Li^+ ions and electrons is facilitated. These effects collectively enhance the interfacial and structural stability, thus accounting for the significant improvements in cycling performance and rate capability.

3 | Conclusion

In summary, this study proposes an efficient and practicable bicarbonate pyrolysis-driven strategy for the interface engineering of Li-rich cathodes. By simultaneously incorporating abundant oxygen vacancies, a protective spinel phase layer, and near-surface metal ion doping into the cathode structure, the proposed approach effectively restrains irreversible oxygen release, suppresses cathode/electrolyte side reactions, and optimizes transport kinetics. These improvements not only contribute to enhanced interfacial stability but also inhibit structural degradation, leading to superior overall performance. Consequently, the modified cathodes deliver significantly improved cycling stability, superior rate capability, and enhanced thermal stability. The strategy is successfully applied to fabricate various types of modified Li-rich cathodes (SK-LR, SNa-LR, and SMg-LR), all of which exhibit enhanced cycling stability compared to the unmodified material. Among them, SK-LR demonstrates the most outstanding cycling durability, achieving an ultrahigh capacity retention of 94.9% after 500 cycles at 1C. Mechanism insights gain through comprehensive characterization and theoretical calculations reveal that the strategy markedly increases the oxygen vacancy formation energy, enhances interfacial/structural stability, and improves ionic/electronic conductivity. This bicarbonate pyrolysis-driven strategy offers a novel insight for designing ultra-stable Li-rich cathodes, demonstrating considerable potential for application in high-energy density LIBs.

Author Contributions

All authors have agreed to the final version of the manuscript.

Acknowledgements

The authors acknowledge funding support from the Natural Science Foundation of Guangxi Province (No. 2025GXNSFAA069428), Guangxi Science and Technology Projects (GUIKE LT2600640010), National Natural Science Foundation of China (Grant Number. 22109031), and Natural Science Foundation of Guangxi Province (No. 2022GXNSFBA035513). During the preparation of this work, the authors used ChatGPT in order to assist with the readability and language of the manuscript. After using this tool, the authors reviewed and edited the content as needed and take full responsibility for the content of the published article.

Funding

Natural Science Foundation of Guangxi Province (No. 2025GXNSFAA069428), Guangxi Science and Technology Projects (GUIKE LT2600640010), National Natural Science Foundation of China (Grant No. 22109031), and Natural Science Foundation of Guangxi Province (No. 2022GXNSFBA035513).

Conflicts of Interest

The authors declare no conflict of interest.

Data Availability Statement

The data that support the findings of this study are available from the corresponding author upon reasonable request.

References

1. W. Jiang, C. Zhang, Y. Feng, et al., "Achieving High Structure and Voltage Stability in Cobalt-Free Li-Rich Layered Oxide Cathodes via Selective Dual-Cation Doping," *Energy Storage Mater* 32 (2020): 37–45.

2. W. Huang, J. Qiu, Z. Zhuo, et al., "A Quasi-Ordered Mn-Rich Cathode with Highly Reversible Oxygen Anion Redox Chemistry," *Journal of the American Chemical Society* 147 (2025): 26218.

3. M. Yoon, Y. Dong, J. Hwang, et al., "Reactive Boride Infusion Stabilizes Ni-Rich Cathodes for Lithium-Ion Batteries," *Nature Energy* 6 (2021): 362–371, https://doi.org/10.1038/s41560-021-00782-0.

4. M. Zhang, L. Qiu, W. Hua, et al., "Formulating Local Environment of Oxygen Mitigates Voltage Hysteresis in Li-Rich Materials," *Advanced Materials* 36 (2024): 2311814, https://doi.org/10.1002/adma.202311814.

5. Z. Liu, Y. Zeng, J. Tan, et al., "Revealing the Degradation Pathways of Layered Li-Rich Oxide Cathodes," *Nature Nanotechnology* 19 (2024): 1821–1830.

6. Z. Xu, X. Guo, X. Zeng, et al., "Coherent Strain-Inhibiting Phase Construction of Lithium-Rich Manganese-Based Oxide Toward High Mechanochemical Stability," *Journal of the American Chemical Society* 147 (2025): 3967–3980, https://doi.org/10.1021/jacs.4c11385.

7. H. Liao, M. Cai, W. Ma, et al., "Carbonated Beverage Chemistry for High-Voltage Battery Cathodes," *Advanced Materials* 36 (2024): 2402739, https://doi.org/10.1002/adma.202402739.

8. Y. Liu, S. Li, J. Li, et al., "Tailoring the Reaction Heterogeneity for Robust Li-Rich Cathodes," *Advanced Materials* 38 (2026): 08120, https://doi.org/10.1002/adma.202508120.

9. Z. Zhu, D. W. Yu, Y. Yang, et al., "Gradient Li-Rich Oxide Cathode Particles Immunized Against Oxygen Release by A Molten Salt Treatment," *Nature Energy* 4 (2019): 1049–1058, https://doi.org/10.1038/s41560-019-0508-x.

10. J. Lee, D. W. Yu, Z. Zhu, et al., "Kinetic Rejuvenation of Li-Rich Li-Ion Battery Cathodes upon Oxygen Redox," *ACS Applied Energy Materials* 3 (2020): 7931–7943, https://doi.org/10.1021/acsaem.0c01315.

11. Y. Ouyang, Y. Zhang, G. Wang, et al., "An In Situ Near-Surface Reconstruction Strategy Endowing Lithium-Rich Oxides With Li/O Dual Vacancies and Spinel-Carbon Dual Coating Layers Toward High Energy Density Cathode," *Advanced Functional Materials* 34 (2024): 2401249, https://doi.org/10.1002/adfm.202401249.

12. Y. Chen, Q. Li, Z. Chen, et al., "Mild Lithium-Rich Manganese-Based Cathodes With the Optimal Activation of Li_2MnO_3 for Stable and High Capacity Lithium-Ion Batteries," *Advanced Functional Materials* 34 (2024): 2411542, https://doi.org/10.1002/adfm.202411542.

13. W. J. Kong, C. Z. Zhao, L. Shen, et al., "Bulk/Interfacial Structure Design of Li-Rich Mn-Based Cathodes for All-Solid-State Lithium Batteries," *Journal of the American Chemical Society* 146 (2024): 28190–28200, https://doi.org/10.1021/jacs.4c08115.

14. C. Zheng, J. Zhang, H. Mao, et al., "Entropic Design of Anionic Site to Improve Anionic Redox Stability in Lithium-Rich Cathode," *Advanced Materials* 36 (2024): 2413785.

15. T. Zeng, M. Yang, F. Sun, et al., "Interface Engineering via Constructing Enhanced Ligand Enables Highly Stable Li-Rich Layered Oxide Cathode," *Advanced Functional Materials* 34 (2024): 2314528, https://doi.org/10.1002/adfm.202314528.

16. X. Han, R. Wu, G. Gao, et al., "Lattice and Local Electronic Structure Modulation Enables Ultra-Long-Life Li-Rich Cathode Materials," *ACS Energy Letters* 9 (2024): 3219–3226, https://doi.org/10.1021/acsenergylett.4c00939.

17. Z. Zhan, W. Peng, L. Yuan, et al., "Quantifying and Inhibiting Manganese Dissolution in Li-Rich Mn-Based Cathode Materials," *ACS Nano* 19 (2025): 40258–40270, https://doi.org/10.1021/acsnano.5c17190.

18. S. Kang, D. Choi, S. Lee, et al., "Surface Vacancy Engineering Re-Routes First-Cycle Redox for Stabilized Li-Rich Layered Cathodes," *Angewandte Chemie International Edition* 65 (2026): 17720, https://doi.org/10.1002/anie.202517720.

19. S. Li, F. Liu, S. Zhang, et al., "Surface Nonbonding Oxygen State Regulation for Reversible Anionic Redox Chemistry in Li-Rich Mn-Based Layered Oxides," *Angewandte Chemie International Edition* 64 (2025): 202424079.

20. H. Zheng, M. Fan, C. Zhang, et al., "Optimizing Oxygen Redox Activity by Local Chemical Disorder Toward Robust Co-Free Li-Rich Cathode With High Voltage Stability," *Advanced Materials* 37 (2024): 2414443, https://doi.org/10.1002/adma.202414443.

21. Y. F. Liu, H. X. Liu, Y. F. Zhu, et al., "Stabilizing Layered Oxide Cathodes Based on Universal Surface Residual Alkali Conversion Chemistry for Rechargeable Secondary Batteries," *Advanced Materials* 37 (2025): 2417540, https://doi.org/10.1002/adma.202417540.

22. Z. Zhu, R. Gao, I. Waluyo, et al., "Stabilized Co-Free Li-Rich Oxide Cathode Particles With An Artificial Surface Prereconstruction," *Advanced Energy Materials* 10 (2020): 2001120, https://doi.org/10.1002/aenm.202001120.

23. Q. Wang, M. Yao, A. Zhu, Q. Wang, H. Wu, and Y. Zhang, "Semi-Metallic Superionic Layers Suppressing Voltage Fading of Li-Rich Layered Oxide Towards Superior-Stable Li-Ion Batteries," *Angewandte Chemie International Edition* 62 (2023): 202309049.

24. K. Jin, L. Li, H. Tian, et al., "Three Birds with One Stone: Reducing Gases Manipulate Surface Reconstruction of Li-Rich Mn-Based Oxide Cathodes for High-Energy Lithium-Ion Batteries," *Energy Storage Materials* 77 (2025): 104202, https://doi.org/10.1016/j.ensm.2025.104202.

25. W. Li, B. Zhao, J. Bai, et al., "Sulfuretted Li- and Mn-Rich Cathode Material with Epitaxial Spinel Stabilizer for Ultra-Long Cycle Li-Ion Battery," *Chemical Engineering Journal* 454 (2023): 140398, https://doi.org/10.1016/j.cej.2022.140398.

26. Y. Ye, S. Yuan, X. Yang, S. Song, and Q. Wang, "Oxygen Vacancies Design of Anionic Site to Optimize Electrode–Electrolyte Interface Properties on a Li-Rich Cathode," *Nano Letters* 25 (2025): 12379–12385, https://doi.org/10.1021/acs.nanolett.5c03025.

27. X. Gao, L. Wang, J. Guo, et al., "Lattice Engineering Toward Extraordinary Structural Stability of High-Performance Single-Crystal Li-Rich Layered Oxides Cathodes," *Advanced Functional Materials* 34 (2024): 2407692, https://doi.org/10.1002/adfm.202407692.

28. G. Wang, C. Xie, H. Wang, et al., "Mitigated Oxygen Loss in Lithium-Rich Manganese-Based Cathode Enabled by Strong Zr–O Affinity," *Advanced Functional Materials* 34 (2024): 2313672, https://doi.org/10.1002/adfm.202313672.

29. B. Qiu, M. Zhang, L. Wu, et al., "Gas–Solid Interfacial Modification of Oxygen Activity in Layered Oxide Cathodes for Lithium-Ion Batteries," *Nature Communications* 7 (2016): 12108, https://doi.org/10.1038/ncomms12108.

30. Y. Yang, Q. Zhu, J. Yang, et al., "Surface Miscible Structure Modulation of Li-Rich Cathodes by Dual Gas Surface Treatment for Super High-Temperature Electrochemical Performance," *Advanced Functional Materials* 33 (2023): 2304979, https://doi.org/10.1002/adfm.202304979.

31. Z. Huang, T. F. Xiong, X. Lin, et al., "Carbon Dioxide Directly Induced Oxygen Vacancy in the Surface of Lithium-Rich Layered Oxides for High-Energy Lithium Storage," *Journal of Power Sources* 432 (2019): 8–15, https://doi.org/10.1016/j.jpowsour.2019.05.069.

32. K. Hu, H. Tang, B. Zheng, et al., "Constructing Targeted Strong $Nb_{4d}-O_{2p}-Li_{2s}$ Configurations to Obtain Excellent Energy Density and Long Life for Li-Rich Cathodes," *Angewandte Chemie International Edition* 64 (2024): 202413563, https://doi.org/10.1002/anie.202413563.

33. R. Zhang, Y. F. Zhou, C. C. Li, et al., "Dislocation Recovery-Recrystallization Enhances Structural Stability of Lithium-Rich Manganese-Based Cathode Materials," *Energy Storage Materials* 84 (2026): 104796, https://doi.org/10.1016/j.ensm.2025.104796.

34. H. Wei, Y. Liu, Y. Luo, et al., "Regulation of Anion Redox Activity via Solid-Acid Modification for Highly Stable Li-Rich Mn-Based Layered Cathodes," *Advanced Functional Materials* 34 (2024): 2307583, https://doi.org/10.1002/adfm.202307583.

35. D. Luo, X. Ding, J. Fan, et al., "Accurate Control of Initial Coulombic Efficiency for Lithium-rich Manganese-based Layered Oxides by Surface Multicomponent Integration," *Angewandte Chemie International Edition* 59 (2020): 23061–23066, https://doi.org/10.1002/anie.202010531.

36. Y. Liu, X. Tang, H. Wang, et al., "Regulating the Multiscale Stability of Li-Rich Cathode Through Lewis Acid Gas Treatment," *Advanced Functional Materials* 34 (2024): 2406947, https://doi.org/10.1002/adfm.202406947.

37. Y. H. Feng, A. M. Rao, J. Zhou, and B. A. Lu, "Selective Potassium Deposition Enables Dendrite-Resistant Anodes for Ultrastable Potassium-Metal Batteries," *Advanced Materials* 35 (2023): 2300886, https://doi.org/10.1002/adma.202300886.

38. P. Yang, L. Shang, H. Wang, et al., "Layered-Spinel Heterogeneous Structure and Oxygen Vacancies Enable Superior Electrochemical Performance for Li-Rich Cathodes," *Angewandte Chemie International Edition* 64 (2025): 202501539.

39. Z. Ye, B. Zhang, T. Chen, et al., "A Simple Gas–Solid Treatment for Surface Modification of Li-Rich Oxides Cathodes," *Angewandte Chemie International Edition* 60 (2021): 23248–23255, https://doi.org/10.1002/anie.202107955.

40. Q. Jiang, X. Li, Y. Hao, et al., "Oxygen-Vacancy-Assisted Dual Functional Surface Coatings Suppressing Irreversible Phase Transition of Li-Rich Layered Oxide Cathodes (Adv. Funct. Mater. 2/2025)," *Advanced Functional Materials* 35 (2025): 2570008, https://doi.org/10.1002/adfm.202570008.

41. J. L. Guo, Y. Q. Lai, X. G. Gao, et al., "Triggering Cationic/Anionic Hybrid Redox Stabilizes High-Temperature Li-Rich Cathodes Materials Via Three-In-One Strategy," *Energy Storage Materials* 69 (2024): 103383, https://doi.org/10.1016/j.ensm.2024.103383.

42. Y. Lou, Z. Lin, J. Shen, et al., "Simultaneous Regulating the Surface, Interface, and Bulk via Phosphating Modification for High-Performance Li-Rich Layered Oxides Cathodes," *Advanced Materials* 37 (2025): 2416136, https://doi.org/10.1002/adma.202416136.

43. Y. C. Liu, Y. Lu, S. H. Jing, et al., "Artificial Anion Vacancies Tailoring Local Oxygen Structure of Li-Rich Cathode for High-Energy and Durable All-Solid-State Batteries," *Energy Storage Materials* 84 (2026): 104808, https://doi.org/10.1016/j.ensm.2025.104808.

44. M. Z. Yang, T. L. Chen, G. R. Wang, et al., "A Surface-To-Interface Boronation Engineering Strategy Stabilizing the O/Mn Redox Chemistry of Lithium-Rich Manganese Based Oxides Towards High Energy-Density Cathodes," *Energy & Environmental Science* 18 (2025): 6168–6179, https://doi.org/10.1039/D4EE04857A.

45. J. J. Marie, R. A. House, G. J. Rees, et al., "Trapped O_2 and the Origin of Voltage Fade in Layered Li-Rich Cathodes," *Nature Materials* 23 (2024): 818–825, https://doi.org/10.1038/s41563-024-01833-z.

46. K. Wang, Y. Chu, Z. Huang, et al., "Unleashing the Kinetic Limitation of Co-Free Li-Rich Mn-Based Cathodes via Ionic/Electronic Dual-Regulation," *Advanced Materials* 37 (2025): 2504642, https://doi.org/10.1002/adma.202504642.

47. X. Sun, C. Qin, B. Zhao, et al., "A Cation and Anion Dual-Doping Strategy in Novel Li-Rich Mn-Based Cathode Materials for High-Performance Li Metal Batteries," *Energy Storage Materials* 70 (2024): 103559, https://doi.org/10.1016/j.ensm.2024.103559.

48. Q. Huang, K. Qiu, Z. Xiao, et al., "Self-Grading and Surface-Preservation to Enhance the Compaction Density and Structural Stability of Li-Rich Mn-Based Cathode," *Advanced Functional Materials* 35 (2025): 2422663, https://doi.org/10.1002/adfm.202422663.

49. S. Li, Y. Liu, Y. Zhang, et al., "Multi-Functionalized Full-Interface Integrated Engineering Towards Highly Reversible Li-rich Mn-Based

Cathode," *Energy Storage Materials* 66 (2024): 103241, https://doi.org/10.1016/j.ensm.2024.103241.

50. J. Meng, W. Hu, Q. Ma, et al., "Mg^{2+}/Al^{3+} Co-doped Li-Rich Manganese-Based Oxides for Boosting Rate Performance and Stability of Lithium-Ion Batteries," *Advanced Functional Materials* 35 (2025): 2501762, https://doi.org/10.1002/adfm.202501762.

Supporting Information

Additional supporting information can be found online in the Supporting Information section.

Supporting File: smll74307-sup-0001-SuppMat.docx.